Fabrication and characterization of single walled carbon nanotubes-iron phthalocyanine nano-composite: surface properties and electron transport dynamics of its self assembled monolayer film†

Isaac Adebayo Akinbulu and Tebello Nyokong*

Received (in Montpellier, France) 25th May 2010, Accepted 3rd August 2010
DOI: 10.1039/c0nj00395f

Nano-composite of single walled carbon nanotubes (SWCNTs) and iron phthalocyanine, peripherally tetra-substituted with diethylaminoethanethiol (complex **2**), was fabricated and characterized by infra red (IR) spectroscopy, X-ray diffraction (XRD) and transmission electron microscopy (TEM). TEM technique gave a convincing image of the nano-composite. Self-assembled monolayer (SAM) film of the composite (SWCNT-**2**-SAM) was formed on gold electrode. Its surface properties were investigated, relative to that of **2**-SAM film, by cyclic voltammetry and scanning electron microscopy (SEM). Electrochemical impedance spectroscopy (EIS) and cyclic voltammetry, using $[Fe(CN)_6]^{3-}$ as redox probe, were used to investigate the dynamics of electron transport in the SWCNT-**2**-SAM film. Lower charge transfer resistance, R_{CT}, of the SWCNT-**2**-SAM modified Au electrode, relative to that of the **2**-SAM modified Au electrode, was an indication of enhanced electron transport in the presence of SWCNT. The SAM film of the nano-composite showed better electrocatalytic behaviour, relative to that of **2**-SAM film, towards the oxidation of the insecticide, carbofuran. The electrode (SWCNT-**2**-SAM) showed good selectivity for carbofuran, in the presence of diazinon (a non-electroactive interferent) and at lower concentration of the electroactive interferents (chlorpyrifos and dichlorfos).

Introduction

Since carbon nanotubes (CNTs) were discovered two decades ago in electric arc-discharge experiments, during the synthesis of fullerene,[1] these one-dimensional nanostructures have attracted unprecedented attention. This is not surprising, considering the wide range of applications of these nano-materials. The discovery of CNTs has revolutionized the design of biosensors, nanoelectronics,[2–5] electrochemical supercapacitors (ESs)[6–8] and electrochemical sensors[9–13] among others. There are also increasing demands for the use of CNTs in hydrogen storage[14–16] and design of fuel cells.[17,18] The unique physical, chemical and electronic properties of these nanostructures make them suitable for these applications. Similarly, metallophthalocyanine (MPc) complexes, containing electroactive metal centers, have attracted tremendous attention; because of their technological applications,[19–21] mainly in the construction of electrochemical sensors. The above applications have also been attributed to the unique physico–chemical, electronic and electrocatalytic properties of these macrocycles.[22,23] Therefore, deliberate combination of these two π-electron-rich systems (CNTs and MPc complexes) will produce a nano-composite of enhanced physical, chemical, electrocatalytic and electronic properties. This underscores our motivation for this study.

Department of Chemistry, Rhodes University, Grahamstown 6140, South Africa. E-mail: t.nyokong@ru.ac.za; Fax: +27 46 6225109; Tel: +27 46 6038260

† Electronic supplementary information (ESI) available: Additional data. See DOI: 10.1039/c0nj00395f

Redox and electrocatalytic properties of SAM film formed from single walled carbon nanotube (SWCNT)-CoPc conjugate have been reported before.[24] However, unlike the present study, the conjugate was formed from pre-formed SAM, making extensive characterization of its molecular make-up impossible before SAM formation. Other reports on SWCNT-MPc conjugates were centered on drop dry method of electrode modification.[25,26]

Synthesis and electrochemical characterization of the MPc complex (FePc complex, peripherally tetra-substituted with diethylaminoethanethiol (complex **2**)), used for the construction of this nano-composite, are reported in this work. The molecular features of the substituent (presence of sulfur and nitrogen groups) (Scheme 1) make it the ideal candidate for the fabrication of this composite.

Tertiary amine status of the nitrogen atom of the substituent (Scheme 1) offers a rich nucleophilic site, facilitating the formation of amide linkage with the carbonyl group of the functionalized SWCNTs (SWCNT-COOH), resulting in the formation of the composite of **2** with SWCNT. The amide bond is expected to be coordinate covalent in nature, since ethyl is not a good leaving group.

The presence of sulfur atom in the substituent satisfies a necessary prerequisite for the formation of SAM film of the nano-composite on gold electrode.

The composite was characterized by IR spectroscopy, X-ray diffraction (XRD) spectroscopy and transmission electron microscopy (TEM). Thin film of the nano-composite was formed on gold electrode by self-assembly technique.

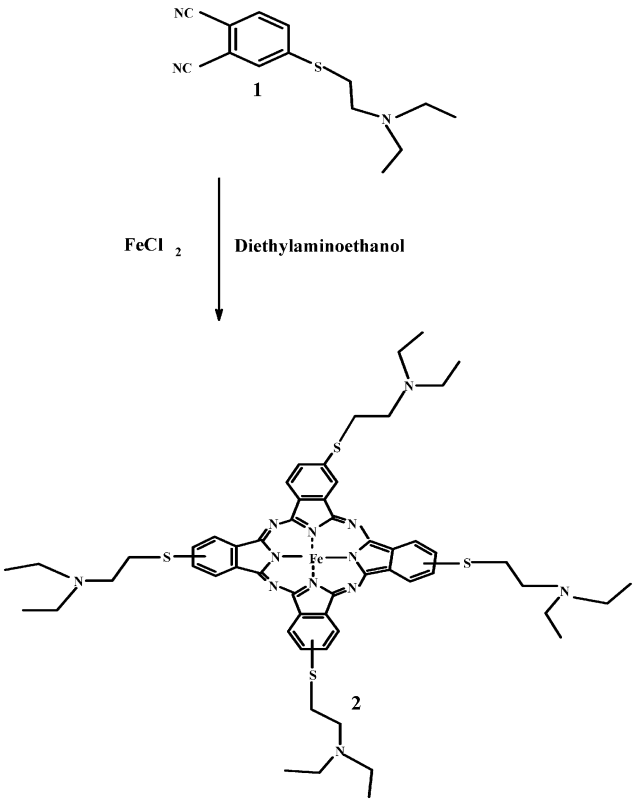

Scheme 1 Synthetic pathway for complex **2**.

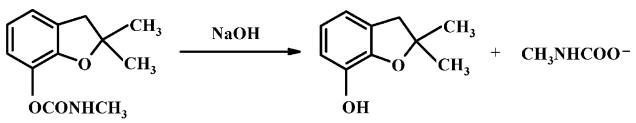

Carbofuran

Scheme 2 Alkaline hydrolysis of carbofuran in 0.5 M NaOH.

This technique is one of the most effective methods of forming stable and reproducible thin films of CNTs[12,27,28] or MPcs.[29–31] SAM film of the composite was characterized by cyclic voltammetry and scanning electron microscopy (SEM). Electrochemical impedance spectroscopy (EIS) and cyclic voltammetry, using $[Fe(CN)_6]^{3-}$ as redox probe, were used to investigate the dynamics of electron transport in the SAM film of the composite. The SAM film was employed for electrocatalytic oxidation of the insecticide, carbofuran. Carbofuran is a systemic carbamate insecticide, used in the control of insects in a wide range of field crops such as soybeans, potatoes and corn. It is highly toxic, with toxicity close to that of parathion and aldicarb;[32] hence its electrocatalytic oxidation is environmentally relevant. Carbofuran is electrochemically inactive, but its hydrolyzed form (Scheme 2) is electroactive. The selectivity of the SWCNT-**2**-SAM film for carbofuran was investigated using diazinon, chlorpyrifos and dichlorvos as potential interferents.

Experimental

Materials

Potassium carbonate, iron(II) chloride tetrahydrate, 2-(diethylaminoethanethiol) hydrochloride, 2-diethylaminoethanol, dicyclohexylcarbodiimide (DCC), single walled carbon nanotubes (SWCNTs, 7–1.2 nm in diameter and 2–20 μm in length), carbofuran, diazinon, chlorpyrifos and dichlorvos were obtained from Sigma-Aldrich. Anhydrous form of iron(II) chloride was obtained by heating the hydrated form in an oven. Tetrabutylammonium tetrafluoroborate ($TBABF_4$) (Aldrich) was used as the electrolyte for electrochemical characterization of complex **2**. Aluminium oxide, WN-3: neutral for column chromatography, was purchased from Sigma-Aldrich. Dimethylformamide (DMF) and dichloromethane (DCM) were obtained from Merck. DMF, DCM, methanol and ethanol were distilled before use. Stock solution of carbofuran (2.0×10^{-3} M) was prepared in freshly distilled methanol because it was sparingly soluble in water, then diluted with water for analyses. Stock solutions of diazinon, chlorpyrifos and dichlorfos, used as interferents, were prepared as discussed for carbofuran. All solutions were prepared with ultrapure water of resistivity 18.2 MΩ cm obtained from a Milli-Q Water system. Electrochemical experiments were carried out in argon-saturated aqueous solutions containing small amounts of methanol from the stock solution of carbofuran. Prior to electrochemical analysis involving carbofuran, a measured volume of the stock solution was hydrolyzed in 0.5 M solution of NaOH. Acetic acid was added to adjust the pH to 4, which gave the best voltammetry response of carbofuran. Also, the SAM film of the nano-composite was stable at this pH.

Electrochemical studies

All electrochemical experiments were performed using Autolab potentiostat PGSTAT 302 (Eco Chemie, Utrecht, The Netherlands) driven by the general purpose Electrochemical System data processing software (GPES, software version 4.9) or BioAnalytical Systems (BAS) model 100B/W Electrochemical Workstation (for rotating disc electrode, RDE, voltammetry). RDE studies were done in the potential range of 0.1 to 0.6 V at 1000 rpm. A conventional three-electrode system was used. The working electrode was a bare glassy carbon electrode (GCE) (for electrochemical characterization of complex **2**) or gold electrode (for formation of SAM films of complex **2** and the nano-composite), Ag|AgCl wire and platinum wire were used as the pseudo reference and auxiliary electrodes respectively. The potential response of the Ag|AgCl pseudo-reference electrode was less than the Ag|AgCl (3 M KCl) by 0.015 ± 0.003 V. Prior to use, the glassy carbon electrode surface was polished with alumina on a Buehler felt pad and rinsed with excess millipore water. The gold electrode surface was also polished in aqueous slurry of alumina on sic-emery paper and subjected to ultrasonic vibration in absolute ethanol to remove residual alumina. The electrode was then etched in hot 'piranha' solution (1 : 3 v/v 30% H_2O_2 and conc. H_2SO_4) for two minutes and rinsed with excess millipore water. It was later scanned in 0.5 M H_2SO_4 between −0.5 to 1.5 V *vs.* Ag|AgCl to obtain a reproducible cyclic voltammetry scan. The real surface area and surface roughness factor of the bare gold electrode were determined using the

conventional methods[33] applying eqn (1) (Randles-Sevcik equation).

$$I_{pa} = (2.69 \times 10^5) n^{\frac{3}{2}} D^{\frac{1}{2}} \upsilon^{\frac{1}{2}} AC \quad (1)$$

where n is the number of electrons transferred (= 1), D (7.6×10^{-6} cm^2 s^{-1}), is the diffusion coefficient of the redox active species ($[Fe(CN)_6]^{3-}$),[33] υ is the scan rate (50 mV s^{-1}) and C (0.01 M) is the bulk concentration of $[Fe(CN)_6]^{3-}$. Geometric surface area of the electrode is 0.020 cm^2. The surface roughness of the electrode was found to be 1.05 (ratio of I_{pa} experimental/I_{pa} theoretical) corresponding to a real electrode area of 0.021 cm^2.

Prior to SAM formation, the polished Au electrode was rinsed with freshly distilled DMF and placed in a solution of the nano-composite (1×10^{-4} M), or complex **2** (1×10^{-4} M), in DMF for 24 h. Gold-coated glass was used for SEM characterization. The glass was immersed in solution of complex **2**, or the nano-composite, in DMF for five days.

Electrochemical impedance spectroscopy measurements were performed with Autolab FRA software, between 1.0 mHz and 10 KHz, using a 5 mV rms sinusoidal modulation, in 1 mM solution of $[Fe(CN)_6]^{3-}$ containing 0.1 M KCl as supporting electrolyte, at the half-wave potential of $[Fe(CN)_6]^{3-}/[Fe(CN)_6]^{4-}$ (0.10 V *versus* Ag|AgCl). A non-linear least squares (NNLS) method based on the EQUIVCRT programme[34] was used for automatic fitting of the obtained EIS data.

Equipment

UV/Vis spectrum was recorded on Shimadzu UV-2550 UV-Vis spectrophotometer. IR spectra were recorded on Perkin-Elmer Spectrum 100 FT-IR spectrometer. Elemental analysis was performed using Vario Elementar Microcube EL111. ^{1}H nuclear magnetic resonance (^{1}H NMR, 400 MHz) was obtained in $CDCl_3$ using Bruker EMX 400 NMR spectrometer. Scanning electron microscope (SEM) images were recorded using Tescan Digital Microscope model. Transmission electron microscope (TEM) images were recorded using JEOL JEM 1210 at 100 KV accelerating voltage. X-ray powder diffraction (XRD) patterns were recorded on a Bruker D8 Discover, equipped with a proportional counter, using Cu-Kα radiation (λ = 1.5405 Å, nickel filter). Samples were placed on a silicon wafer slide and data recorded within the range $2\theta = 5^\circ$ to 60°, scanning at 1° min^{-1} with a filter time-constant of 2.5 s per step and a slit width of 6.0 mm. X-ray diffraction data were fitted using Eva (evaluation curve fitting) software, while analysis of data was done using International Center Diffraction Data (ICDD) database.

Synthesis

Complex 2. Compound **1** was synthesis using the method reported recently.[35] Synthesis of complex **2** was carried out according to the method reported for the cobalt analogue.[35] A mixture of compound **1** (0.40 g, 1.54 mmol) and anhydrous iron(II) chloride (0.048 g, 0.38 mmol) was refluxed in 2-(diethylaminoethanol) (1.2 ml) for 12 h under nitrogen. Thereafter, the mixture was cooled to room temperature and treated with excess MeOH : H_2O (1 : 1) to precipitate the crude deep green product. The product was filtered and dried in air. Purification was achieved using column chromatography with neutral alumina as column material and DCM/methanol (10 : 1) as eluent. Yield: 1.24 g (74%) (Found: C, 56.62%; H, 5.61%; N, 14.12%; S, 11.30%; Calc. for $C_{56}H_{68}N_{12}S_4Fe.CH_2Cl_2$: C, 57.09%; H, 5.78%; N, 14.27%; S, 10.88%); UV-Vis (DCM): λ_{max} (nm) (logε): 704 (5.3), 584 (4.6), 422 (5.0), 354 (5.3); IR: ν_{max}/cm^{-1}: 2972 (CH_2 stretch), 1602 (aromatic C=C stretch), 1460, 1393 (CH_2 and CH_3 bends), 826, 746 (aromatic C–H bends).

Formation of SWCNT-COOH. SWCNTs were purified and oxidized to form SWCNT-COOH by adding raw SWCNTs (100 mg) to a mixture of HNO_3 and H_2SO_4 (3 : 1)[36] The resulting suspension was stirred at a temperature of 70 °C for 2 h. The final mixture was cooled to room temperature and washed with excess millipore water until a pH of 5 was obtained. The purified SWCNTs (SWCNT-COOH) were dried in an oven for 12 h.

Formation of SWCNT-2 nano-composite. SWCNT-COOH (10 mg) was added to 4 ml of freshly distilled DMF. The mixture was sonicated for 1 h to aid the solubility of SWCNT-COOH in DMF. DCC (1 mg) was added to the resulting mixture to convert the carboxyl groups of the SWCNT-COOH to active carbodiimide esters. The mixture was stirred under nitrogen for 72 h. Thereafter, 10 mg of complex **2** was added to the black solution and stirred for 72 h under nitrogen. Nucleophilic reaction between the activated –COOH of SWCNT-COOH and tertiary amine group ($-NR_3$) of the substituent of complex **2** (Scheme 1) resulted in the formation of amide bond (coordinate covalent), linking the units together in the nano-composite. The composite was dried in an oven for 12 h and characterized using IR spectroscopy, TEM and XRD techniques.

Results and discussion

Synthesis and characterization of complex 2

Synthesis. The synthetic route for complex **2** is shown in Scheme 1. Cyclotetramerization of compound **1** took place in the presence of $FeCl_2$ to form complex **2**. Purification of complex **2** was accomplished using column chromatography on alumina. The complex was soluble in solvents such as DMF, DCM and DMSO.

Characterization of complex **2** was carried out using IR and UV-Vis spectroscopies as well as elemental analysis. The results obtained were consistent with the predicted structure shown in Scheme 1. Formation of complex **2** was confirmed by the disappearance of the sharp C≡N vibration at 2229 cm^{-1} of **1**.

Spectral and electrochemical characterization. The UV-Vis spectrum of 5.50×10^{-6} M of complex **2** in DCM shows a broad Q-band at 704 nm (Fig. 1, ESI†). A broad Q-band is characteristic of aggregation in MPc complexes. The bands at 422 and 354 nm are usually associated with charge transfer and B-band respectively.

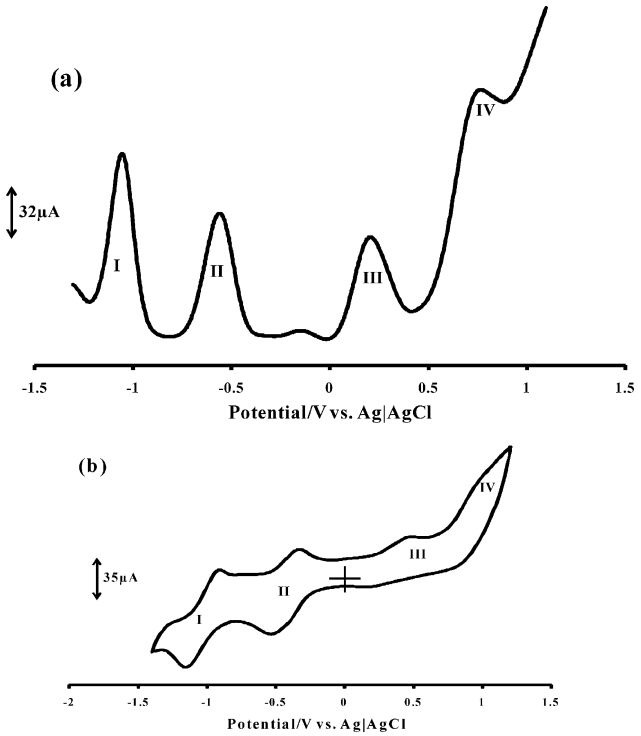

Fig. 1 (a) Square wave and (b) cyclic voltammetry profiles of 1×10^{-3} M of complex **2** in DMF, Frequency = 10 Hz, amplitude = 50 mV, step potential = 5 mV, scan rate = 100 mV s^{-1} *versus* Ag|AgCl.

Fig. 1a and b show the square wave and cyclic voltammetry profiles of 1×10^{-3} M of complex **2** in freshly distilled DMF containing 0.1 M $TBABF_4$ as supporting electrolyte. Four redox processes can be identified. Process **I** is a quasi-reversible (with anodic to cathodic peak difference, ΔE, larger than 90 mV obtained for ferrocene standard) ring-based reduction, assigned to $Fe^{I}Pc^{-2}/Fe^{I}Pc^{-3}$ species ($E_{1/2}$ = −1.03 V *vs.* Ag|AgCl), in comparison with literature[37–40] (Table 1). Processes **II** is a metal-based reduction, associated with $Fe^{II}Pc^{-2}/Fe^{I}Pc^{-2}$ species ($E_{1/2}$ = −0.43 V *vs.* Ag|AgCl)[37,38] (Table 1). Its cathodic to anodic current ratio is near unity, but quasi-reversible (ΔE > 90 mV obtained for ferrocene standard). Process **III** showed a very weak cathodic component. It is assigned to metal-based oxidation and formation of $Fe^{III}Pc^{-2}/Fe^{II}Pc^{-2}$ species ($E_{1/2}$ = +0.33 V *vs.* Ag|AgCl). Process **IV** is an irreversible ring-based oxidation, attributed to $Fe^{III}Pc^{-1}/Fe^{III}Pc^{-2}$ species (E_p = 0.97 V *vs.* Ag|AgCl)[39,40] (Table 1). Ring substituent oxidation is also expected for alkylthio substituted phthalocyanines.

Characterization of SWCNT-2 nano-composite

IR spectroscopic characterization. Infra red spectroscopy was used to investigate the molecular make-up of the nano-composite, relative that of its individual units. IR spectrum of SWCNT-COOH (Fig. 2a, ESI†) shows a broad peak, characteristic of O–H stretch of COOH, near 3300 cm^{-1}, while bands at 1702 and 1228 cm^{-1} were attributed to C=O and C–O stretches of COOH, respectively. For complex **2** (Fig. 2b, ESI†), bands at 2968 and 1600 cm^{-1} are attributed to aliphatic C–H and aromatic C=C stretches, respectively. Peaks at 1460 and 1393 cm^{-1} are signatures of CH_2 and CH_3 deformations, while bands at 822 and 746 cm^{-1} can be associated with aromatic C–H bends, for **2**. For the mixture of complex **2** and SWCNT-COOH (Fig. 2c, ESI†), bands at 2970 and 1460 cm^{-1} are associated with aliphatic C–H stretch and CH_2 or CH_3 bend respectively, which are features of complex **2** component of the mixture. The band at 1708 cm^{-1} is characteristic of C=O stretch of COOH in the SWCNT-COOH component of the mixture. IR spectrum of the nano-composite (SWCNT-**2**) (Fig. 2d, ESI†) shows bands that suggest successful fabrication of the composite. Peak at 3327 cm^{-1} can be ascribed to O–H stretch (from the free COOH of SWCNT-COOH). Broad nature, characteristic of O–H stretch of COOH, was not observed in Fig. 2d (ESI†), due to likely overlap with aliphatic C–H stretch. The strong band at 1625 cm^{-1} is characteristic of C=O stretch of amide, confirming formation of the nano-composite. C=O stretch of free COOH in SWCNT-COOH was observed at 1702 cm^{-1} (Fig. 2a, ESI†). The difference in position of C=O stretch can be attributed to resonance effect, which weakens the C=O stretch of amides and conjugated carbonyls; hence appears at lower frequency than normal C=O stretch. The rest of the bands can be associated with SWCNT or complex **2**.

The amide bond in the nanocomposite is expected to be coordinate covalent in nature, because ethyl is not a good leaving group. Enhanced electrophilicity of the carboxyl group of SWCNT-COOH, in the presence of DCC, facilitated nucleophilic attack by the nitrogen atom of the tertiary amine functionality of complex **2** (Scheme 3). Formation of amide bond between tertiary amines and acids has been reported in a patent on the synthesis of carbon acid amides.[41] Formation of amide bond was initiated and promoted by the activation of the acids, using suitable activating agents, such as the coupling agent (DCC) used in this work.

X-ray diffraction characterization. Structural properties of the nano-composite, relative to that of its constituent units (SWCNT-COOH and complex **2**), were investigated using

Table 1 Summary of peak and half wave potentials, in V *vs.* Ag|AgCl, of complex **2** in comparison with that of previously reported thio-substituted FePc complexes. Values were recorded in DMF containing $TBABF_4$ unless otherwise stated

Complex	$Fe^{I}Pc^{-2}/Fe^{I}Pc^{-3}$	$Fe^{II}Pc^{-2}/Fe^{I}Pc^{-2}$	$Fe^{III}Pc^{-2}/Fe^{II}Pc^{-2}$	$Fe^{III}Pc^{-1}/Fe^{III}Pc^{-2}$	References
Complex **2**	−1.03	−0.43	+0.33	+0.97	TW[c]
FeODEAETPc[a]	−0.9	−0.35	+0.26	+0.87	39
FeTDMPc[a,b]	−0.84	−0.53	+0.62	+1.01	40

[a] ODEAETPc = octa diethylaminoethanethio phthalocyanine and TDMPc = tetra dodecylmercapto phthalocyanine. [b] Values recorded in DCM, using $TBABF_4$. [c] TW = this work.

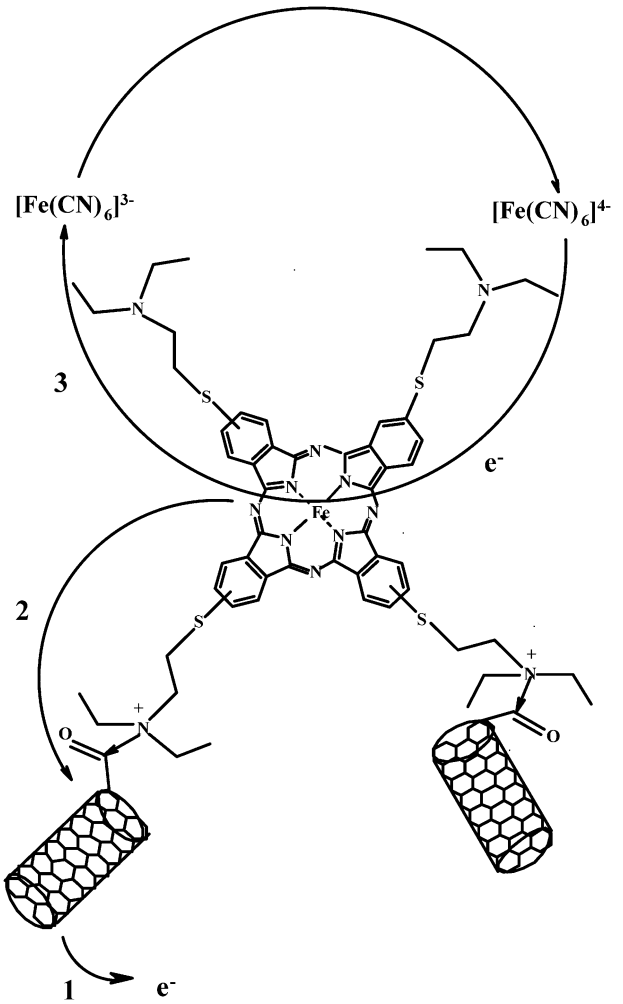

Scheme 3 Hypothetical model illustrating electron transport mechanism within SWCNT-**2**-SAM film.

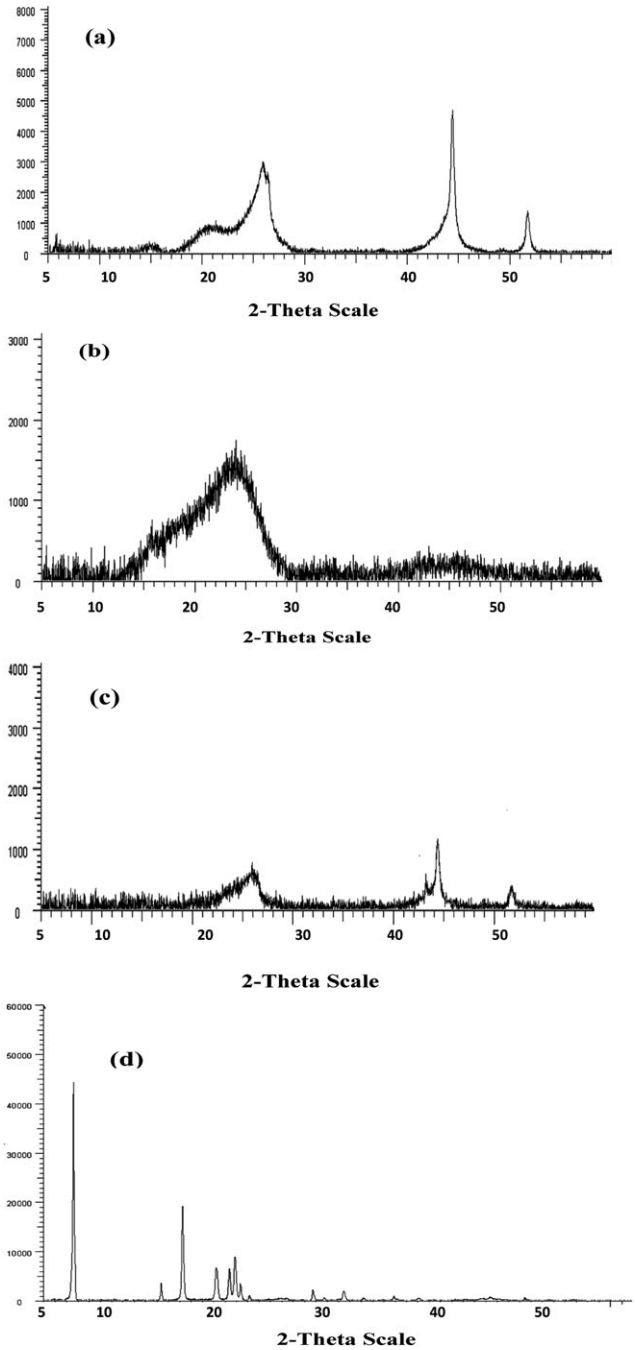

Fig. 2 XRD spectra of (a) SWCNT-COOH, (b) Complex-**2**, (c) Mixture of SWCNT-COOH and complex-**2** and (d) SWCNT-**2** nano-composite.

X-ray diffraction technique. Changes in nature and positions of peaks on a given XRD spectrum are reflective of changes in structural features of the sample under consideration. Fig. 2a–d show the XRD spectra of SWCNT-COOH, complex **2**, mixture of SWCNT-COOH and complex **2**, and SWCNT-**2** nano-composite, respectively. In Fig. 2a (for SWCNT-COOH), the broad ($2\theta = 20.4^\circ$ and 25.9°) and sharp ($2\theta = 44.4^\circ$ and 51.8°) peaks are indicative of the amorphous and crystalline natures of the SWCNT-COOH, respectively. Using ICDD database, the peak at $2\theta = 25.9^\circ$ (approximately 26°) can be ascribed to (002) d-spacing of the SWCNT-COOH,[42,43] while peaks at $2\theta = 44.4^\circ$ and 51.8° are characteristic of (100)[42] and (200)[43] reflections of carbon of the SWCNT-COOH, respectively. The peak at $2\theta = 24.1^\circ$ was the only pronounced peak on the XRD spectrum of **2** (Fig. 2b). This peak is close to the (002) reflection of carbon.[43] Importantly, the broad nature of this peak underlines the substantial amorphous nature of complex **2**. XRD spectrum of the mixture of SWCNT-COOH and complex **2** (Fig. 2c) was dominated by peaks characteristic of the structural properties of the SWCNT-COOH component. As discussed above, peaks at approximately 26°, 44.4° and 51.7° were signatures of (002), (100) and (200) reflections of carbon of the SWCNT-COOH, respectively.[42,43] The peak near 26° overlaps that of complex **2**. XRD spectrum of the nano-composite (Fig. 2d) was significantly different from that obtained for the individual components or ordinary mixture of the units of the nano-composite. There was complete disappearance of reflections {(002), (100) and (200)} originating from planes within the SWCNT-COOH. Also, peaks associated with reflections from planes within complex **2** have disappeared completely. These observations, convincingly, suggest successful fabrication of

the nano-composite. XRD spectrum in Fig. 2d was analyzed using ICDD database. Miller indices (hkl) for the observed peaks (110) (7.6°), (220) (15.3°), (310) (17.2°), (400) (21.8°), (330) (22.3°) and (321) (28.7°) suggest reflections from planes within the composite are different from that within its constituent units (SWCNT-COOH and complex **2**), confirming the formation of the composite. Importantly, intensities of some of the peaks on the XRD spectrum of the nano-composite were relatively higher than the intensities of the peaks on the XRD spectrum of any of its constituent units. This suggests reflecting planes within the composite pass through areas of higher electron densities, compared to that within its constituent units. This is expected, since electron density of the composite is a re-enforcement of that of its individual components.

Transmission electron microscopic characterization. TEM technique offered a microscopic view of the nano-composite. Fig. 3a shows the TEM image of SWCNT-COOH. Importantly, image obtained after the formation of the nano-composite (Fig. 3b) was distinctly different from that shown in Fig. 3a. Fig. 3b shows a nano-composite, with complex **2** attached continuously to the walls of the carbon nanotubes. Possible structures of the nano-composite are shown in Fig. 4.

Formation and surface properties of SAM film of the nano-composite

Strong interaction between sulfur atoms of the nano-composite and gold resulted in formation of its SAM film (SWCNT-**2**-SAM) on gold electrode. SAM film of **2** (**2**-SAM) was also formed on gold electrode *via* similar mechanism. Surface properties of SWCNT-**2**-SAM film were investigated, within the context of that of **2**-SAM, in order to elucidate the effects of the presence of the SWCNT on such properties.

Microscopic properties. SEM technique was used to investigate the microscopic nature of the SAM film of the nano-composite on gold. The film was formed on gold-coated glass, in place of gold electrode. Fig. 5a shows the SEM image of gold-coated glass before SAM formation. The image shows a rough gold-coated surface. Fig. 5b and c are the SEM images of **2**-SAM and SWCNT-**2**-SAM films on gold-coated glass, respectively. The differences in structural properties of the self-assembled species (complex **2** and the nano-composite) can be observed. SWCNT-**2**-SAM film (Fig. 5c) has structural features different from that of **2**-SAM. The difference is attributed to the presence of SWCNT in the composite.

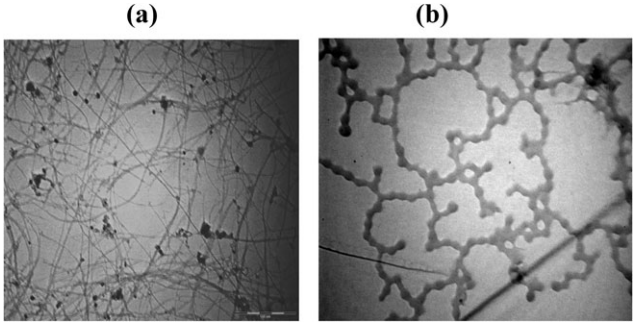

Fig. 3 TEM images of (a) short sections of SWCNT-COOH (×10000) and (b) SWCNT-**2** nanocomposite (×80000).

Cyclic voltammetry properties. Cyclic voltammetry was used to investigate the redox properties of the SAM film of the nano-composite and that of **2**. Voltammetry responses of bare, **2**-SAM and SWCNT-**2**-SAM modified gold electrodes were investigated in (i) 0.1 M KOH, (ii) 1 mM $CuSO_4$ containing 0.5 M H_2SO_4, and (iii) 1 mM ferrous ammonium sulfate $(Fe(NH_4)(SO_4)_2$ containing 1 mM perchloric acid ($HClO_4$). Considerable blocking of these processes was observed on the SAM modified gold electrodes, confirming the formation of the SAM films.

Fig. 6a shows the cyclic voltammetry responses of bare, **2**-SAM and SWCNT-**2**-SAM modified gold electrode in 0.1 M KOH. There was complete inhibition of gold oxidation (at +0.37 V *vs.* Ag|AgCl on bare Au electrode) with substantial decrease in intensity of gold oxide stripping peak (at 0.02 V *vs.* Ag|AgCl on bare Au electrode). The degree of inhibition of this process was evaluated by estimating the ion barrier factor for each SAM, using eqn (2).[33]

$$\Gamma_{ibf} = 1 - \frac{Q_{SAM}}{Q_{Bare}} \qquad (2)$$

where Q_{SAM} and Q_{Bare} are the total charges under the reduction peak (gold oxide stripping peak) for the SAM modified (1.80×10^{-6} C and 3.19×10^{-6} C for **2**-SAM and SWCNT-**2**-SAM respectively) and bare (1.82×10^{-5} C) gold electrodes respectively. Values of Γ_{ibf} obtained were 0.90 and 0.82 for **2**-SAM and SWCNT-**2**-SAM respectively. The closeness of these values to unity suggests closely packed SAMs, with slight defects. The slightly higher value of Γ_{ibf} obtained for **2**-SAM can be attributed to the densely packed, crystalline nature of the SAM film. Presence of SWCNT in the SAM film of the nanocomposite may affect this behavior. Interestingly, SEM images of these films (Fig. 5) show such structural differences.

Voltammetry responses of bare and SAM modified gold electrodes in 1 mM $CuSO_4$, containing 0.5 M H_2SO_4, are shown in Fig. 6b. The redox processes on bare gold surface (under potential deposition and stripping of Cu) were completely blocked on the SAM modified gold electrodes, confirming the formation of the SAM films. Redox process ($E_{1/2}$ = +0.2 V *versus* Ag|AgCl) observed on **2**-SAM modified gold electrode can be attributed to Fe^{3+}/Fe^{2+} species of adsorbed complex **2**. ΔE for this process is near zero, expected for adsorbed species. Redox process for SWCNT-**2**-SAM modified gold electrode were observed at E_p = −0.09 V and $E_{1/2}$ = −0.22 V *versus* Ag|AgCl. These are, respectively, assigned to Fe^{3+}/Fe^{2+} and Fe^{2+}/Fe^{+} redox processes of complex **2** unit of the composite. The observation of the former at less positive potential, compared to complex **2** alone, suggests better electron transfer processes in the SWCNT-**2**-SAM film. This is investigated later in this study.

Fig. 6c shows the cyclic voltammetry profiles of bare and SAM modified gold electrodes in 1 mM ferrous ammonium sulfate ($Fe(NH_4)(SO_4)_2$, containing 1 mM perchloric acid). The quasi-reversible $[Fe(H_2O)_6]^{3+}/[Fe(H_2O)_6]^{2+}$ redox process

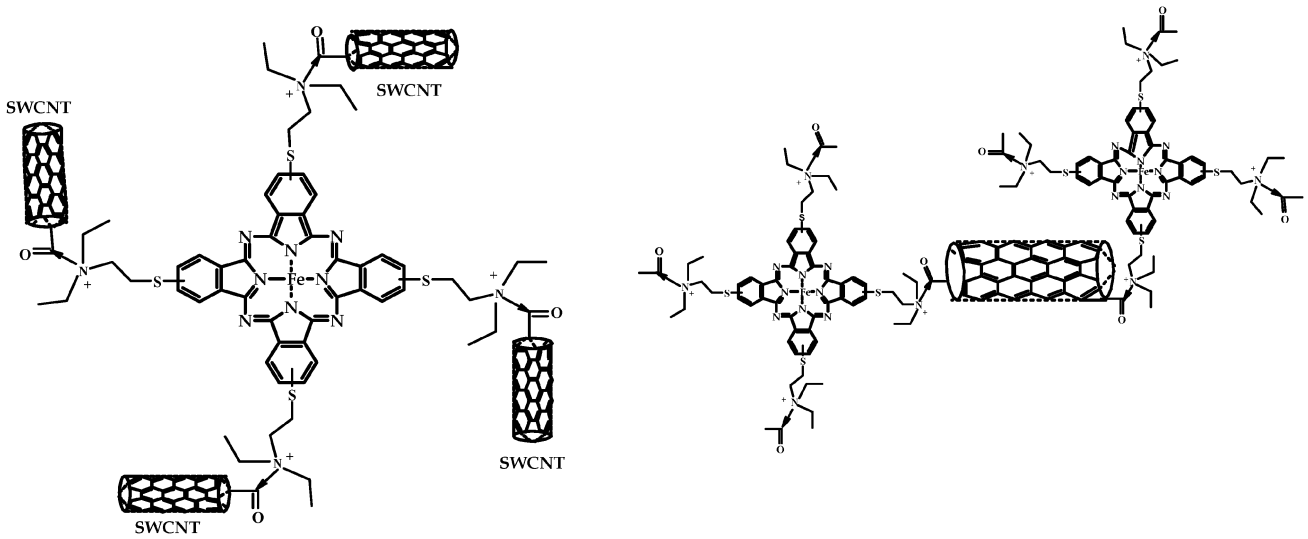

Fig. 4 Possible structures of SWCNT-**2** composite.

on bare gold electrode was completely persivated on **2**-SAM film. However, on SWCNT-**2**-SAM film, this process was observed, but less resolved than that on bare gold electrode. Since the value of Γ_{ibf} obtained for this film (0.82) suggests minimal defects in the SAM, voltammetry trace of Fe^{3+}/Fe^{2+} redox process, observed on this film, may be attributed to better electron transport within this film, relative to **2**-SAM film. Interestingly, XRD spectrum of the nano-composite (Fig. 2d) suggests the composite has higher electron density than complex **2**. If this is evaluated within the context of the good electrical conductivity of SWCNT, better electron transport should be expected in the SWCNT-**2**-SAM film.

Metal-based redox processes of these films, in pH 4 buffer solution, provided more understanding of their redox properties. There was considerable stability of these films at this pH value, hence its relevance.

Fig. 7a shows the cyclic voltammetry profile of **2**-SAM modified gold electrode in pH 4 buffer solution. The redox process at $E_{1/2}$ = +0.22 V *versus* Ag|AgCl is attributed to Fe^{3+}/Fe^{2+} species. The cyclic voltammetry trace in Fig. 7b shows the Fe^{3+}/Fe^{2+} redox process (on SWCNT-**2**-SAM gold electrode) at $E_{1/2}$ = +0.18 V *versus* Ag|AgCl. The difference in potential, compared to Fig. 6b, can be attributed to differences in media. Interestingly, anodic to cathodic peak differences of the Fe^{3+}/Fe^{2+} redox process were 147 and 34 mV *versus* Ag|AgCl on **2**-SAM and SWCNT-**2**-SAM modified gold electrode respectively, supporting the claim that electron transport may be enhanced in the presence of SWCNT. Also, this process was more resolved on SWCNT-**2**-SAM modified gold electrode than on **2**-SAM film.

Values of surface coverage were estimated for the **2**-SAM and SWCNT-**2**-SAM films using eqn (3).

$$\Gamma_{SAM} = \frac{Q}{nFA} \qquad (3)$$

where Q is the background corrected charge under the anodic peaks of the Fe^{3+}/Fe^{2+} redox processes in Fig. 7a (2.2×10^{-7} C) (**2**-SAM) and 7b (2.6×10^{-7} C) (SWCNT-**2**-SAM), n is the number of electron transferred (which is 1), F is faraday's constant and A is the effective surface area of the electrode (0.021 cm^2). Values obtained were 1.09×10^{-10} and 1.30×10^{-10} mol cm^{-2} for **2**-SAM and SWCNT-**2**-SAM modified gold electrodes, respectively. The value of Γ_{SAM} for **2**-SAM is consistent with that expected for a monolayer of MPc-SAM (1×10^{-10} mol cm^{-2}) lying flat on the electrode surface.[44] The relatively higher value of Γ_{SAM} for SWCNT-**2**-SAM modified gold electrode can be attributed to attachment of SWCNT (Fig. 3b).

Fig. 7c shows the cyclic voltammetry traces of SWCNT-**2**-SAM modified gold electrode in pH 4 buffer at different scan rates (50–450 mV s^{-1} *versus* Ag|AgCl). The inset shows the plot of anodic peak current *versus* scan rate. Linear dependence of peak current on scan rate suggests surface-confirment of the SWCNT-**2** species on the electrode.

Electron transport dynamics of the SWCNT-2-SAM film

Dynamics of electron transport within the SWCNT-**2**-SAM film was investigated by cyclic voltammetry and EIS, using $[Fe(CN)_6]^{3-}$ as redox probe. The role of the SWCNT in electron transport was evaluated by comparing electron transfer process in the SWCNT-**2**-SAM film with that in **2**-SAM film.

Cyclic voltammetry traces in Fig. 8 show the responses of bare, **2**-SAM and SWCNT-**2**-SAM modified gold electrodes in 1 mM solution of $[Fe(CN)_6]^{3-}$, containing 0.1 M KCl supporting electrolyte. Anodic and cathodic peak currents of the Fe^{3+}/Fe^{2+} redox process were higher on bare Au than that observed on any of the SAM modified gold electrodes. However, cathodic to anodic peak separation, ΔE, for this process was narrower on the SWCNT-**2**-SAM modified gold electrode (70 mV *versus* Ag|AgCl) than on the bare (83 mV *versus* Ag|AgCl) or **2**-SAM modified gold electrode (130 mV *versus* Ag|AgCl). This is consistent with enhanced electrical conductivity of the film in the presence of SWCNT. Lower anodic and cathodic current responses of the Fe^{3+}/Fe^{2+} redox process, observed on SWCNT-**2**-SAM (or **2**-SAM) modified gold electrode, relative to that on the

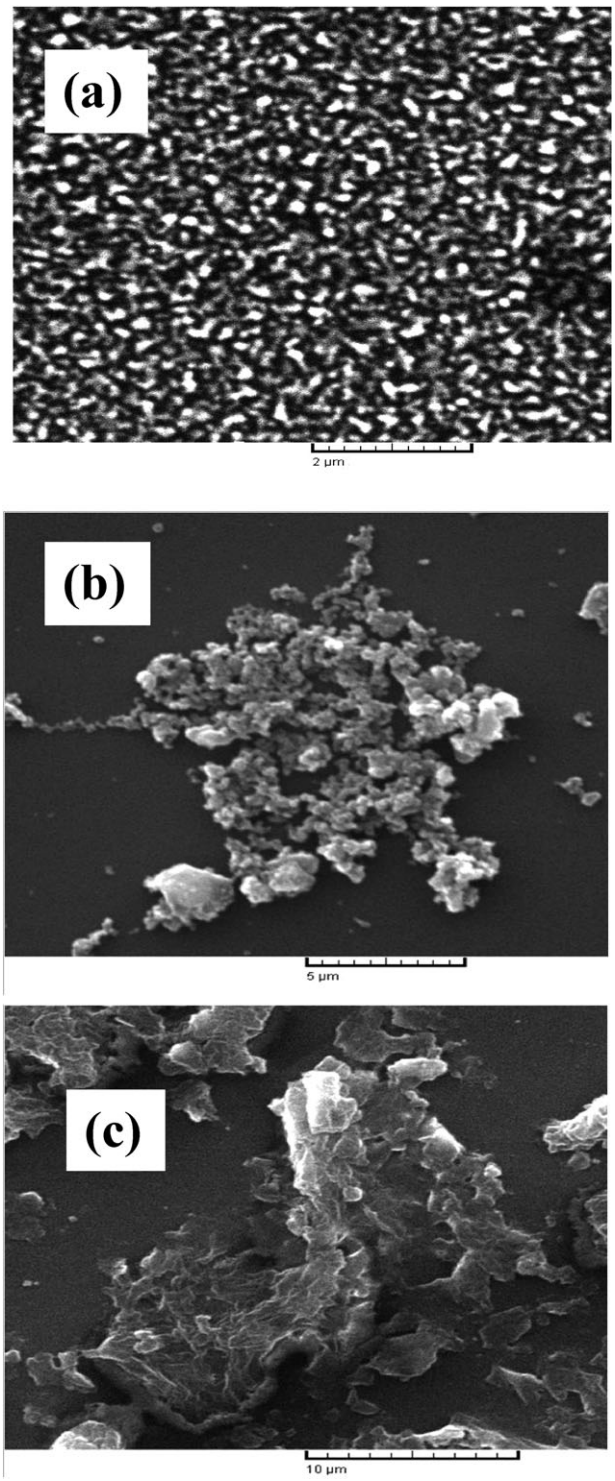

Fig. 5 SEM images of (a) bare gold-coated glass, (b) **2**-SAM and (c) SWCNT-**2** SAM modified gold-coated glass.

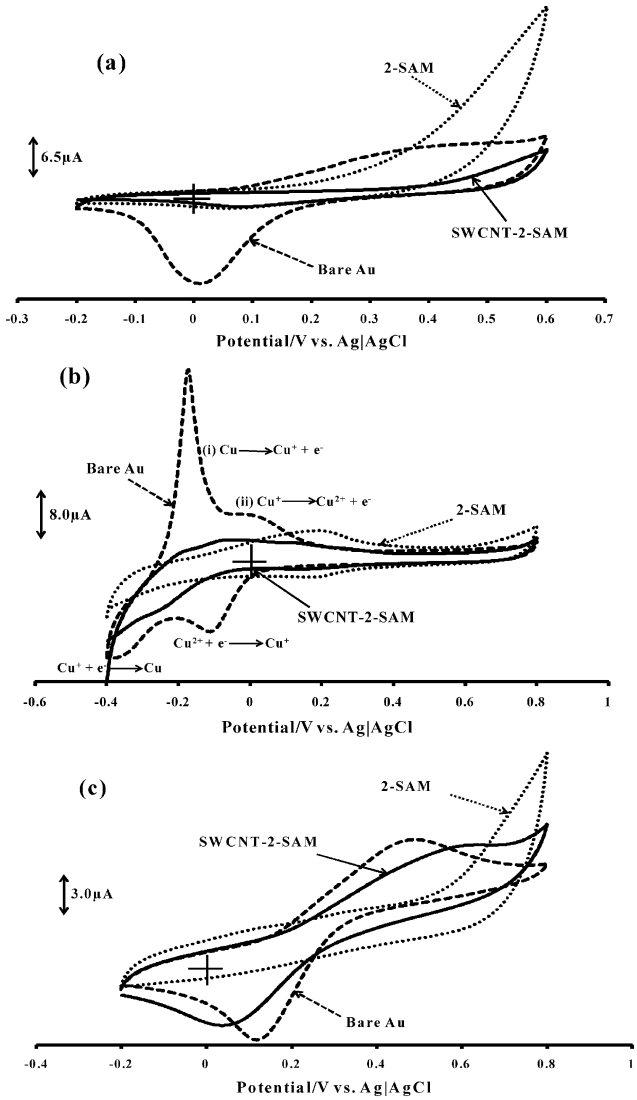

Fig. 6 Cyclic voltammetry profiles of bare (dashed line) and MPc-SAM film modified gold electrodes in (a) 0.1 M KOH solution, (b) 1 mM $CuSO_4$ solution containing 0.5 M H_2SO_4 and (c) 1 mM $Fe(NH_4)(SO_4)_2$ solution containing 1 mM $HClO_4$. Scan rate: 25 mV s^{-1} *versus* Ag|AgCl.

bare gold electrode, can be attributed to effect of electrons tunneling the film.

EIS offered better understanding of the relevance of the SWCNT unit of the nano-composite film in electron transport. Fig. 9a shows the fitted impedance spectra of bare, **2**-SAM and SWCNT-**2**-SAM gold electrodes in 1 mM solution of $[Fe(CN)_6]^{3-}$, containing 0.1 M KCl supporting electrolyte. All the impedance spectra showed semi-circular behavior, characteristic of charge transfer-limited impedance, in the high-frequency region, and a linear portion, associated with a purely diffusion-controlled phenomenon, in the low-frequency region. The circuit in Fig. 9a (inset) was used to interpret the experimental data generated from the impedance spectra in Fig. 9a. R_S is the resistance of the electrolyte solution between the reference and the working electrodes, R_{CT} is the charge transfer resistance, Z_W is mass-transfer or Warburg impedance and C_{dl} is the double-layer capacitance, that mimicks the capacitance of the electrochemical double layer of the cell. Values of these parameters are shown in Table 2.

R_S is within narrow range (0.47 to 0.81 KΩ). This is expected, since electrode modification does not significantly affect this parameter. Also, Z_W (impedance associated with diffusion of analyte to the electrode surface) are, expectedly,

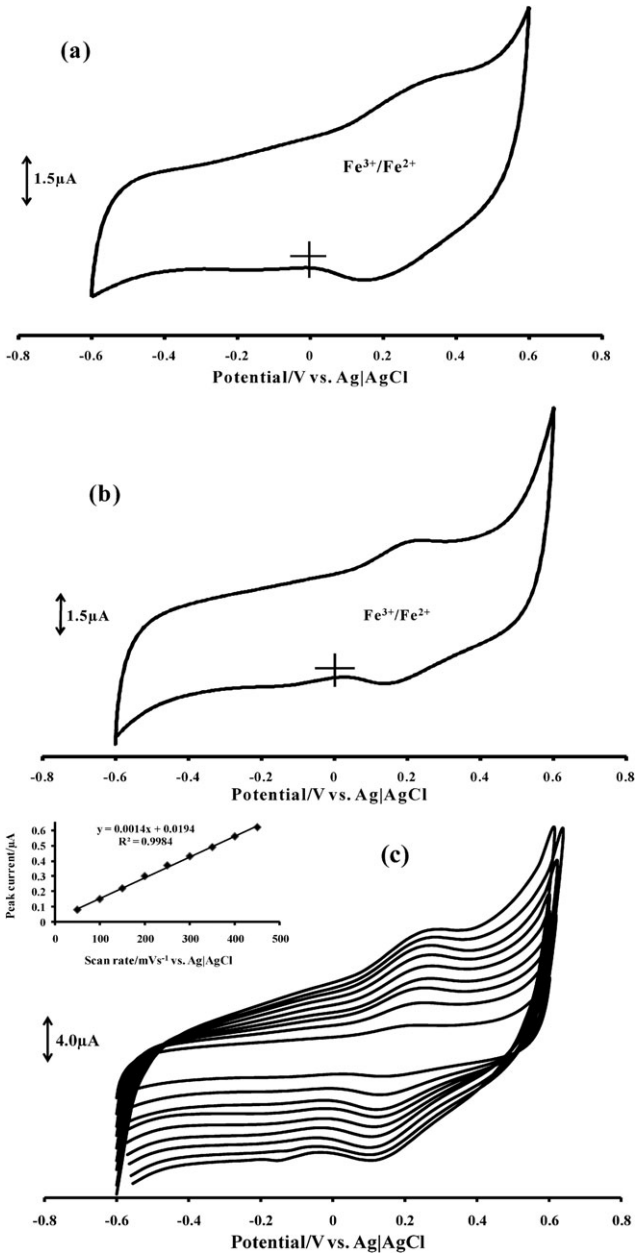

Fig. 7 Cyclic voltammograms of (a) **2**-SAM, (b) SWCNT-**2**-SAM modified gold electrodes in pH 4 buffer solution. Scan rate = 50 m Vs^{-1} *versus* Ag|AgCl. (c) Cyclic voltammograms of SWCNT-**2**-SAM modified gold electrode at different scan rate (50–450 m Vs^{-1}), inset is plot of peak current against scan rate.

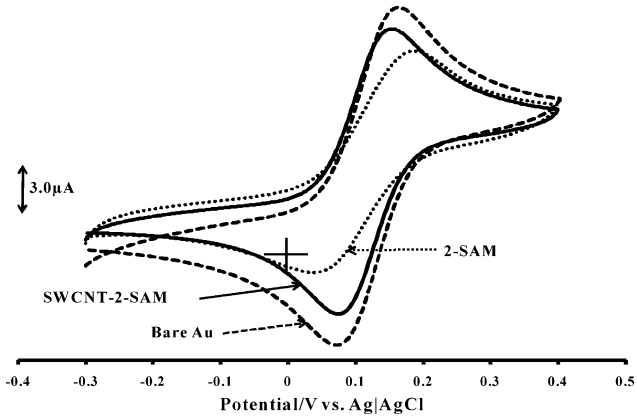

Fig. 8 Cyclic voltammetry traces of bare, **2**-SAM and SWCNT-**2**-SAM modified gold electrodes in 1 mM solution of $[Fe(CN)_6]^{3-}$ containing 0.1 M KCl supporting electrolyte. Scan rate: 25 mV s^{-1} *versus* Ag|AgCl.

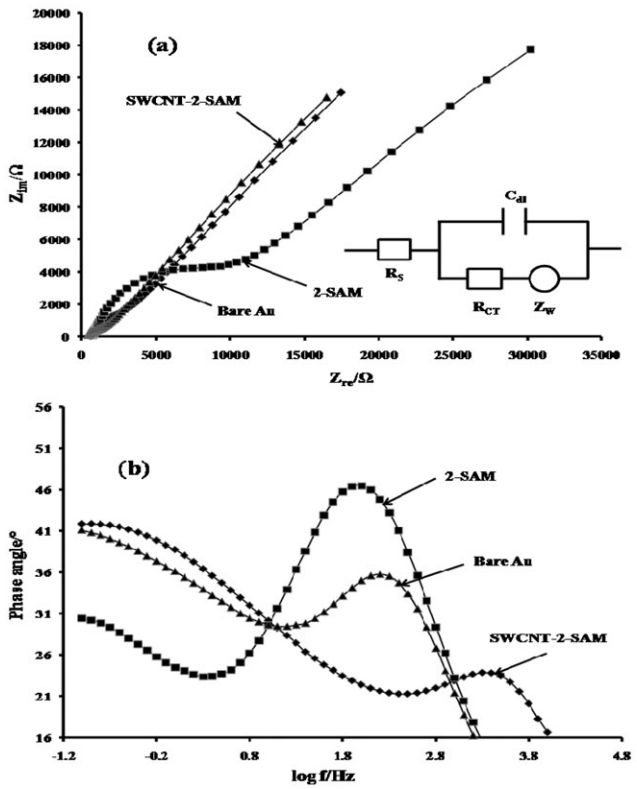

Fig. 9 (a) Fitted impedance spectra obtained for bare and SAM modified gold electrodes in 1 mM solution of $[Fe(CN)_6]^{3-}$, containing 0.1 M KCl as supporting electrolyte. Applied potential = 0.10 V *versus* Ag|AgCl. Inset = suggested equivalent circuit for the impedance spectra. (b) Bode plots derived from the impedance spectra.

not affected by electrode modification. Each of the electrodes has 'n' value less than 1. This is consistent with the non-ideal capacitive nature of the electrodes. Values of C_{dl} are also a reflection of the conducting nature of the SAM film; SWCNT-**2**-SAM modified gold electrode has the lowest value of capacitance (0.14 μF). Values of charge transfer resistance, R_{CT}, were the most informative of the electrical conductivity of the electrodes. SWCNT-**2**-SAM modified gold electrode has the lowest charge transfer resistance. R_{CT} for **2**-SAM modified gold electrode (6.10 KΩ) was ten folds that for SWCNT-**2**-SAM modified gold electrode (0.62 KΩ). High electrical conductivity of SWCNT, coupled with enhanced electron density of the nano-composite, may have facilitated better electron transport in the SWCNT-**2**-SAM film, resulting in lowest R_{CT}.

Bode plots (Fig. 9b) (phase angle *versus* log f) gave a clear understanding of the difference in nature of the electrode|electrolyte interfaces. Phase angles and frequencies,

Table 2 Summary of impedance data obtained for the bare and SAM modified gold electrodes at applied potential of 0.1 V *versus* Ag|AgCl

Electrode	R_{CT}/KΩ	R_S/KΩ	Cdl/μF	$Z_W/\Omega s^{-1/2}$	*n*	Phase angle/°	*f*/Hz
Bare gold	1.42 ± 0.04	0.60 ± 0.01	0.65 ± 0.02	5.67 ± 0.1 × 10^{-5}	0.70 ± 0.01	35.8	158
2-SAM	6.10 ± 0.30	0.81 ± 0.024	0.56 ± 0.02	4.30 ± 0.2 × 10^{-5}	0.80 ± 0.01	46.0	100
SWCNT-**2**-SAM	0.62 ± 0.02	0.47 ± 0.01	0.14 ± 0.01	5.74 ± 0.1 × 10^{-5}	0.60 ± 0.17	23.8	2512

corresponding to the maxima of the curves in Fig. 9b represent the relaxation processes of the electrode|electrolyte interfaces. This pair of values was significantly affected by the nature of the electrode|electrolyte interface (Table 2). For bare gold electrode, phase angle and frequency corresponding to the maximum of the curve were 35.8° and 158 Hz respectively. These values were different in the presence of **2**-SAM (46° and 100 Hz) and SWCNT-**2**-SAM (23.8° and 2512 Hz) films (Table 2), suggesting different nature of electrode|electrolyte interfaces. Also, positions of phase peaks are consistent with the cyclic voltammograms in Fig. 8, corroborating our explanation thereof. A phase peak at 2512 Hz for SWCNT-**2** modified gold electrode was the highest; suggesting the Fe^{3+}/Fe^{2+} redox process has the highest rate constant on this film. This agrees perfectly with the narrowest peak splitting, ΔE, (70 mV *versus* Ag|AgCl) (Fig. 8) observed for this process on SWCNT-**2** modified gold electrode, relative to that on the bare (83 mV *versus* Ag|AgCl) and **2**-SAM modified (130 mV *versus* Ag|AgCl) gold electrodes.

Based on the impact of SWCNT on electron transport, evidenced from the values of R_{CT} (0.62 KΩ) and phase peak (2512 Hz), the mechanism in Scheme 3 is proposed, to illustrate electron transport within the SWCNT-**2**-SAM film. Process (1) represents tunneling of electron from the SCWNT to gold electrode (the latter not shown), facilitating electron transport from the central metal of complex **2** (process (2)), resulting in the oxidation of Fe^{2+}Pc to Fe^{3+}Pc. Process (3) illustrates heterogeneous electron transfer involving the metal center of complex **2** and the reversible $[Fe(CN)_6]^{3-/4-}$ redox process. Electrocatalytic property of this film, towards the oxidation of carbofuran, discussed later in this work, can also be explained using the above hypothetical model.

Electrocatalytic use of the SWCNT-2-SAM film

The SAM film of the nano-composite was used for electrocatalytic oxidation of the insecticide, carbofuran. Alkaline hydrolysis of carbofuran is shown in Scheme 2. Fig. 10 shows the cyclic voltammetry profiles of bare and SAM modified gold electrodes in 200 μM solution of carbofuran (pH 4). The best voltammetry response of the insecticide was observed on SWCNT-**2**-SAM modified gold electrode (2.07 μA, 0.44 V). This can be attributed to high electrical conductivity of SWCNT in the SWCNT-**2**-SAM film. The response of the insecticide on **2**-SAM modified gold electrode (0.95 μA, 0.53 V) was slightly better than that on bare gold electrode (0.74 μA, 0.67 V). These current responses were background-corrected.

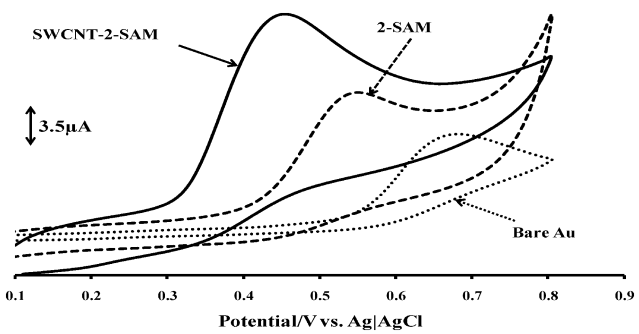

Fig. 10 Cyclic voltammetry traces of bare and SAM modified gold electrodes in 200 μM solution of carbofuran (pH 4). Scan rate: 100 mV s^{-1} *versus* Ag|AgCl.

Mechanism of electrocatalysis of carbofuran on SWCNT-**2**-SAM modified gold electrode was investigated using rotating disc electrode voltammetry (RDE). RDE voltammogram for the oxidation of 200 μM solution of carbofuran (pH 4), at rotation speed of 1000 rpm, is shown in Fig. 11. Inset is the Tafel plot (plot of η *versus* log I_k) obtained from the RDE voltammogram. I_k is the kinetic current corrected for mass transport ($I_k = (I \times I_L)/(I_L - I)$) and η is overpotential. I_L and *I* are the limiting current (current obtained at 0.60 V *vs.* Ag|AgCl) and the current at the foot of the wave respectively. Linear relationship between I_k and overpotential is expressed by eqn (4) (Tafel equation).

$$\eta = a + b \log I_k \quad (4)$$

where *a* is the Tafel constant, relating the exchange current density (I_o) and *b* is the Tafel slope. Eqn (5) expresses the relationship between *a* and I_o

$$a = (2.3RT/\alpha nF) \times \log I_o \quad (5)$$

The value of I_o is a measure of the intrinsic rate of electron transfer between the analyte and the electrode. The expression for Tafel slope is shown in eqn (6).[45]

$$b = 2.3RT/\alpha n_a F \quad (6)$$

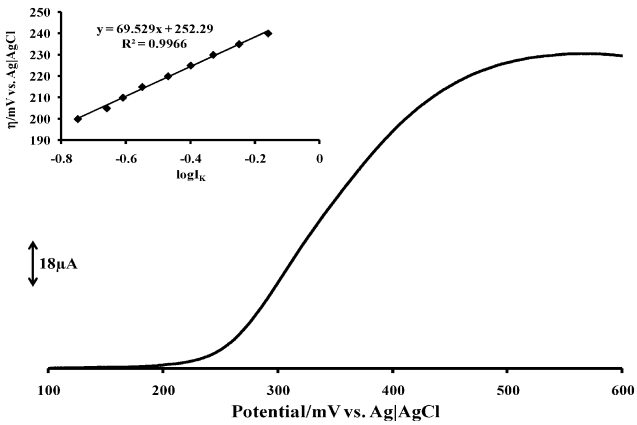

Fig. 11 RDE Voltammogram for the oxidation of 200 μM carbofuran (pH 4), at 100 rpm, on SWCNT-**2**-SAM modified gold electrode, scan rate: 20 mV s^{-1} *vs.* Ag|AgCl. Inset: Tafel plot obtained from the RDE voltammogram.

Table 3 Values of amperometric selectivity coefficient for SWCNT-**2**-SAM modified gold electrode with respect to 200 μM carbofuran

Interferent	Diazinon			Chlorpyrifos			Dichlorvos		
Concentration/μM	100	200	300	100	200	300	100	200	300
K_{amp}	4.8×10^{-4}	9.7×10^{-4}	1.2×10^{-3}	1.1×10^{-3}	1.9×10^{-3}	1.8×10^{-1}	1.1×10^{-3}	7.4×10^{-2}	8.6×10^{-2}

where n_a is the number of electron involved in the rate-determining step and α is the electron transfer coefficient. A Tafel slope of 69.5 mV/decade was obtained. A Tafel slope close to 118 mV/decade indicates the transfer of a first one-electron is rate determining. A Tafel slope close to 59 mV/decade suggests a fast first electron transfer is followed by a slow chemical step. Thus the observed Tafel slope (69.5 mV/decade) denotes a slow chemical step (polymerization of the oxidation product of carbofuran) is preceded by a fast first electron transfer step in the oxidation of carbofuran on the SWCNT-**2**-SAM modified gold electrode. Substrate-catalyst interaction is also ruled out. Thus, electrocatalytic oxidation of carbofuran, on the SAM film of the nano-composite, occured *via* outer sphere mechanism (eqn (7) and (8)). Oxidation potential of carbofuran on this film (+0.44 V *versus* Ag|AgCl) suggests the involvement of Fe^{3+}/Fe^{2+} redox couple in catalysis. This process was observed on SWCNT-**2**-SAM modified gold electrode in pH 4 buffer solution ($E_{1/2}$ = +0.18 V *versus* Ag|AgCl) (Fig. 7b).

$$\text{SWCNT-Fe}^{2+}\text{Pc} \rightarrow \text{SWCNT-Fe}^{3+}\text{Pc} + e^- \quad (7)$$

$$\text{SWCNT-Fe}^{3+}\text{Pc} + \text{RO}^- \rightarrow \text{SWCNT-Fe}^{2+}\text{Pc} + \text{RO} \quad (8)$$

where RO corresponds to carbofuran.

A value of 0.85 was obtained for α, suggesting high probability of product formation. In principle, the value of α is between 0 and 1. It is a measure of the symmetry of the activation energy barrier in a redox reaction coordinate. The closer to unity the value of α, the higher the chance of product formation.

Sensitivity and selectivity studies

Sensitivity of the SWCNT-**2**-SAM modified gold electrode, with respect to detection of carbofuran, was investigated using different concentrations of the analyte (50–500 μM). Current response of carbofuran is linearly related to concentration (Fig. 3, ESI†) within the range investigated. The regression equation of the linear plot is shown in eqn (9), with $R^2 = 0.9996$

$$I_p = 0.011[\text{carbofuran}] \pm 0.003 \quad (9)$$

The sensitivity of the electrode is 0.52 A mol^{-1} L cm^{-2} (slope of the plot/area of the electrode), with detection limit of 8.2×10^{-7} mol/L, determined using 3σ criterion[46] (where σ is the standard deviation of the blank). This value is close to that (5.0×10^{-8} mol/L) reported[47] for detection of carbofuran at disposable heated screen-printed carbon electrode, using differential pulse voltammetry (DPV). The lower value of detection limit associated with the latter can be attributed to the more sensitive nature of DPV, relative to cyclic voltammetry.

The mixed solution method,[48] using diazinon, chlorpyrifos and dichlorvos as interferents, was used to investigate the selectivity of the electrode for carbofuran. These interferents are organophosphate pesticides, normally employed for the same purpose as carbofuran, thus the possibility of their presence in the same environmental samples as carbofuran. Interestingly, mechanism of their pesticidal actions and toxicities is closely related to that of carbofuran (inhibition of cholinestarase activity). Concentrations of carbofuran (200 μM) was kept constant while that of each interferent varied (100–300 μM). Values of amperometric selectivity coefficients (K_{amp}), a measure of the degree of interference, were determined using eqn (10).

$$K_{amp} = \left(\frac{I_{mixture}}{I_{carbofuran}} - 1\right)\frac{[\text{carbofuran}]}{[\text{interferent}]} \quad (10)$$

where $I_{mixture}$ and $I_{carbofuran}$ are the background corrected current responses of carbofuran in the presence and absence of interferent, respectively. K_{amp} value within order of magnitude higher than 10^{-3} denotes strong interference, while value close to 10^{-3} indicates weak interference. Value less than 10^{-3} suggests no interference. Values of K_{amp}, obtained for different concentrations of interferents, are shown in Table 3. Table 3 shows that, at concentration less than or equal to that of carbofuran, diazinon did not interfere with the response of the electrode, while the selectivity of the electrode for carbofuran was weakly affected by the presence of chlorpyrifos, within this concentration range. At higher concentration than that of carbofuran, diazinon showed very weak interference, while chlorpyrifos interfered strongly. Dichlorvos interfered weakly with the selectivity of the electrode at concentration lower than that of carbofuran, but at higher or same concentration as carbofuran, the electrode lost its selectivity for carbofuran.

Difference in degree of interference is closely related to the molecular features of the interferents. Dichlorvos and chlorpyrifos are halogenated organophosphate pesticides, thus may undergo electrochemical reduction at the carbon atoms bearing the halogens. The carbon atom of the vinyl group, containing the two chloro groups (structure not shown), is the possible electroactive position in dichlorvos,[49] while the carbon atoms, bearing the chloro groups, in the heterocyclic ring, are the likely electroactive points in chlorpyrifos. Diazinon does not posses the above structural features, thus the insignificant degree of interference observed in the presence of this insecticide.

Conclusions

Fabrication and characterization of SWCNT-**2** nano-composite are reported. Surface properties and dynamics of electron transport of its SAM film were investigated. Spectroscopic (IR and XRD) and microscopic (TEM) properties of

the nano-composite, relative to that of its individual units, were a confirmation of its successful fabrication. Structural properties of this composite, revealed by its XRD spectrum, showed a marked departure from that of its constituent units, justifying its formation. Surface properties of the SAM film of the SWCNT-**2** composite were significantly affected by the presence of SWCNT. Electron transport within this film was positively influenced by the high electrical conductivity of SWCNT. The SWCNT-**2**-SAM film exhibited better electrocatalytic property than **2**-SAM film, resulting in less positive oxidation potential and amplification of current signal of the insecticide, carbofuran. RDE voltammetry revealed electrocatalytic oxidation of carbofuran on this film occurred *via* outer sphere mechanism. Also, the electrode showed good sensitivity and selectivity for carbofuran, making it a potential electrochemical sensor for this insecticide, under similar condition used in this work.

Acknowledgements

This work was supported by the Department of Science and Technology (DST) and National Research Foundation (NRF) of South Africa through DST/NRF South African Research Chairs Initiative for Professor of Medicinal Chemistry and Nanotechnology and Rhodes University.

References

1 S. Iijima, *Nature*, 1991, **56**, 354.
2 S. J. Tans, A. R. M. Verschueren and C. Dekker, *Nature*, 1998, **393**, 49.
3 Y. Nakayama and S. Akita, *Synth. Met*., 2001, **117**, 207.
4 H. Dai, J. H. Hafner, A. G. Rinzler, D. T. Colbert and R. E. Smalley, *Nature*, 1996, **384**, 147.
5 J. Kong, N. R. Franklin, C. Zhou, M. G. Chapline, S. Peng, K. Cho and H. Dai, *Science*, 2000, **287**, 622.
6 C. S. Li, D. Z. Wang, T. X. Liang, X. F. Wang and L. Ji, *Mater. Lett*., 2004, **58**, 3774.
7 B. Zhang, J. Liang, C. L. Xu, B. Q. Wei, D. B. Ruan and D. H. Wu, *Mater. Lett*., 2001, **51**, 539.
8 H. J. Ahn, J. I. Sohn, Y. S. Kim, H. S. Shim, W. B. Kim and T. Y. Seong, *Electrochem. Commun*., 2006, **8**, 513.
9 C. E. Banks, R. R. Moore, T. J. Davies and R. G. Compton, *Chem. Commun*, 2004, **1804**.
10 L. Sheeney-Haj-Ichia, B. Basnar and I. Willner, *Angew. Chem., Int. Ed*., 2005, **44**, 78.
11 J. J. Gooding, *Electrochim. Acta*, 2005, **50**, 3049.
12 J. J. Gooding, R. Wibowo, J. Liu, W. Yang, D. Losic, S. Orbions, F. J. Meams, J. G. Shapter and D. B. Hibbert, *J. Am. Chem. Soc*., 2003, **125**, 9006.
13 F. Patolsky, Y. Weizmann and I. Willner, *Angew. Chem., Int. Ed*., 2004, **43**, 2113.
14 S. M. Lee, K. S. Park, Y. C. Choi, Y. S. Park, J. M. Bok, D. J. Bae, K. S. Nahm, Y. G. Choi, S. C. Yu, N.-G. Kim, T. Frauenheim and Y. H. Lee, *Synth. Met*., 2000, **113**, 209.
15 P.-X. Hou, S.-T. Xu, Z. Ying, Q.-H. Yang, C. Liu and H.-M. Cheng, *Carbon*, 2003, **41**, 2471.
16 H.-M. Cheng, Q.-H. Yang and C. Liu, *Carbon*, 2001, **39**, 1447.
17 M. Carmo, V. A. Paganin, J. M. Rosolenb and E. R. Gonzalez, *J. Power Sources*, 2005, **142**, 169.
18 R. P. Raffaelle, B. J. Landi, J. D. Harris, S. G. Bailey and A. F. Hepp, *Mater. Sci. Eng., B*, 2005, **116**, 233.
19 *The porphyrin Handbook*, ed. K. M. Kadish, K. M. Smith and R. Guilard, Academic Press, Boston, 2003, vol. 15–20, ch. 97–122.
20 *Phthalocyanines Properties and Applications*, ed. C. C. Leznoff and A. B. P. Lever, VCH publishers, New York, 1989–1996, vol. 1–4.
21 N. B. McKeown, in *Phthalocyanine Materials: Synthesis, Structure and Functions*, Cambridge University Press, Cambridge, 1998.
22 *Encyclopedia of Sensors*, ed. K. I. Ozoemena, T. Nyokong, C. A. Grimes, E. C. Dickey and M. V. Pishko, (Chapter E, and related references), American Scientific Publishers, California, 2006, vol. 3, p. 157.
23 P. Vasuvedan, N. Poughat and A. K. Shuklat, *Appl. Organomet. Chem*., 1996, 591.
24 K. I. Ozoemena, T. Nyokong, D. Nkosi, I. Chambrier and M. J. Cook, *Electrochim. Acta*, 2007, **52**, 4132.
25 D. A. Geraldo, C. A. Togo, J. Limson and T. Nyokong, *Electrochim. Acta*, 2008, **53**, 8051.
26 T. Mugadza and T. Nyokong, *Electrochim. Acta*, 2009, **54**, 6347.
27 L. Su, F. Gao and L. Mao, *Anal. Chem*., 2006, **78**, 2651.
28 P. Diao and Z. Liu, *J. Phys. Chem. B*, 2005, **109**, 20906.
29 T. R. E. Simpson, D. A. Russell, I. Chamber, M. J. Cook, A. B. Horn and S. C. Thorpe, *Sens. Actuators, B*, 1995, **29**, 353.
30 M. J. Cook, *Pure Appl. Chem*., 1999, **71**, 2145.
31 K. I. Ozoemena, T. Nyokong and P. Westbroek, *Electroanalysis*, 2003, **15**, 1762.
32 US Environmental Protection agency, Office of Pesticide Programs.
33 *Electroanalytic Chemistry*, ed. H. O. Finklea, A. J. Bard and I. Rubinstein, Marcel Dekker, New York, 1996, vol. 19, pp. 109–335.
34 B. Boukamp, *Solid State Ionics*, 1986, **20**, 31.
35 I. A. Akinbulu and T. Nyokong, *Polyhedron*, 2010, **29**, 1257.
36 J. Liu, A. G. Rinzler, H. Dai, J. H. Hafner, R. K. Bradley, P. J. Boul, A. Lu, T. Iverson, K. Shelimov, C. B. Huffman, F. Rodriguez-Macias, T. Y.-S. Shon, R. Lee, D. T. Colbert and R. E. Smalley, *Science*, 1998, **280**, 1253.
37 A. B. P. Lever, E. R. Milaeva and G. Speier, in *The redox chemistry of metallophthalocyanines in solution*, ed. C. C. Leznoff, A. B. P. Lever, Phthalocyanines: Properties and Applications, VCH, New York1993, vol. 3, ch. 1.
38 M. L'Her and A. Pondaven, in *Redox Properties and Electrochemistry of Phthalocyanines*, ed. K. M. Kadish, K. M. Smith and R. Guilard, Academic Press, New York, Porphyrin Handbook, phthalocyanine properties and materials, 2003, vol. 16, ch. 104.
39 I. A. Akinbulu and T. Nyokong, *Polyhedron*, 2009, **28**, 2831.
40 B. O. Agboola, K. I. Ozoemena and T. Nyokong, *Electrochim. Acta*, 2006, **51**, 4379.
41 K. Daniel and A. Volker, *Patent cooperation treaty*, PCT/EP/011145, 2006.
42 M. Terrones, W. K. Hsu, A. Schwoerer, K. Prassides, H. W. Kroto and D. R. Walton, *Appl. Phys. A: Mater. Sci. Process*., 1998, **66**, 307.
43 Y. Zhang, X. Sun, L. Pan, H. Li, Z. Sun, C. Sun and B. K. Tay, *J. Alloys Compd*., 2009, **480**, L17.
44 J. H. Zagal, M. A. Guilppi, C. Depretz and D. Lelievre, *J. Porphyrins Phthalocyanines*, 1999, **3**, 355.
45 A. J. Bard and L. R Faulkner, *Electrochemical Methods: Fundamentals and Applications*, John Wiley & Sons, Inc., New York, 2nd edn, 2001.
46 J. C. Miller, J. N. Miller and P. J. Worsfold, *Statistics for Analytical Chemists*, Horwood, Chichester, 1984.
47 W. Hang, S. Jian-Jun, W. Yan-Min, L. Xiao and C. Guo-Na, *Analyst*, 2008, **133**, 1619.
48 R. I. Stefan, J. F. van Staden and H. Y. Aboul-Enein, *Electrochemical Sensors in Bioanalysis*, Marcel Dekker, New York, 2001.
49 A. J. Fry and M. A. Mitnick, *J. Am. Chem. Soc*., 1969, **91**, 6207.

